remote sensing

Article

Integrating Multi-Point Geostatistics, Machine Learning, and Image Correlation for Characterizing Positional Errors in Remote-Sensing Images of High Spatial Resolution

Liang Xin [1,2], Wangle Zhang [3,*], Jianxu Wang [4], Sijian Wang [1] and Jingxiong Zhang [4]

[1] Shanghai Surveying and Mapping Institute, Shanghai 200063, China; xinliang8764@163.com (L.X.); wangsijian2016@163.com (S.W.)
[2] Department of Surveying and Geo-Informatics, Tongji University, 1239 Siping Road, Yangpu, Shanghai 200092, China
[3] College of Geological Engineering and Geomatics, Chang'an University, Xi'an 710054, China
[4] School of Geodesy and Geomatics, Wuhan University, Wuhan 430079, China; 2016301610320@whu.edu.cn (J.W.); jxzhang@whu.edu.cn (J.Z.)
* Correspondence: zhangwl@whu.edu.cn

Abstract: Remote-sensing images of high spatial resolution (HSR) are valuable sources of fine-grained spatial information for various applications, such as urban surveys and governance. There is continuing research on positional errors in remote-sensing images and their impacts in geoprocessing and applications. This paper explores the combined use of multi-point geostatistics (MPS), machine learning—in particular, generalized additive modeling (GAM)—and computer-image correlation for characterizing positional errors in images—in particular, HSR images. These methods are employed because of the merits of MPS in being flexible for non-parametric and joint simulation of positional errors in X and Y coordinates, the merits of GAM in being capable of handling non-stationarity in-positional errors through error de-trending, and the merits of computer-image correlation in being cost-effective in furnishing the training data (TD) required in MPS. Procedurally, image correlation is applied to identify homologous image points in reference-test image pairs to extract image displacements automatically in constructing TD. To cope with the complexity of urban scenes and the unavailability of truly orthorectified images, visual screening is performed to clean the raw displacement data to create quality-enhanced TD, while manual digitization is used to obtain reference sample data, including conditioning data (CD), for MPS and test data for performance evaluation. GAM is used to decompose CD and TD into trends and residuals. With CD and TD both de-trended, the direct sampling (DS) algorithm for MPS is applied to simulate residuals over a simulation grid (SG) at 80 m spatial resolution. With the realizations of residuals and, hence, positional errors generated in this way, the means, standard deviation, and cross correlation in bivariate positional errors at SG nodes are computed. The simulated error fields are also used to generate equal-probable realizations of vertices that define some road centerlines (RCLs), selected for this research through interpolation over the aforementioned simulated error fields, leading to error metrics for the RCLs and for the lengths of some RCL segments. The enhanced georectification of the RCLs is facilitated through error correction. A case study based in Shanghai municipality, China, was carried out, using HSR images as part of generalized point clouds that were developed. The experiment results confirmed that by using the proposed methods, spatially explicit positional-error metrics, including means, standard deviation, and cross correlation, can be quantified flexibly, with those in the selected RCLs and the lengths of some RCL segments derived easily through error propagation. The reference positions of these RCLs were obtained through error correction. The positional accuracy gains achieved by the proposed methods were found to be comparable with those achieved by conventional image georectification, in which the CD were used as image-georectification control data. The proposed methods are valuable not only for uncertainty-informed image geolocation and analysis, but also for integrated geoinformation processing.

check for updates

Citation: Xin, L.; Zhang, W.; Wang, J.; Wang, S.; Zhang, J. Integrating Multi-Point Geostatistics, Machine Learning, and Image Correlation for Characterizing Positional Errors in Remote-Sensing Images of High Spatial Resolution. *Remote Sens.* **2023**, *15*, 4734. https://doi.org/10.3390/rs15194734

Academic Editor: Jon Atli Benediktsson

Received: 10 August 2023
Revised: 21 September 2023
Accepted: 26 September 2023
Published: 27 September 2023

Keywords: positional errors; multi-point geostatistics (MPS); generalized additive modeling (GAM); image correlation; generalized point clouds; high spatial resolution (HSR); training data (TD); conditioning data (CD); variograms; road centerlines

---

1. Introduction

In remote sensing and GIScience, research on errors in geospatial information and analyses aims to describe, model, propagate, visualize, and manage errors systematically through suitable metrics and methods [1–10]. For positional errors, in particular, there has been an impressive accumulation of work investigating the aforementioned topics [11–31]. With the advent of high spatial resolution (HSR) remote-sensing images, the emerging technology of the generalized point cloud dataset [32], and growing demands for high-accuracy geospatial information, research on positional errors in images and geospatial data and their impacts upon image co-registration and other applications is becoming increasingly important, as reflected in relevant literature [33–44].

This research focuses on modeling positional errors in remote-sensing images, especially those of HSR, to facilitate further studies on uncertainty in image-based information extraction and applications. Positional errors refer to the differences between measured and reference (assumed true) coordinates of the objects concerned (i.e., image pixels, in the context of this research). They are bivariate in X and Y coordinates for horizontally positioned points. A closer look into related issues is carried out.

Well-known positional-error descriptors include error ellipses for points and epsilon error bands for lines [20,25,30]. There has also been work on local descriptors of positional errors in 2D [45] and 3D [46]. However, such error descriptors do not lend themselves to modeling spatial uncertainty in spatial queries and analyses involving two or more points. This is due to the presence of spatial correlation in positional errors, which precludes the simple extension of error ellipses to modeling errors in lines (e.g., road centerlines) and areas (e.g., land parcels) by applying the law of variance and covariance propagation [10]. A more sensible method is stochastic simulation, whereby equal-probable realizations of the underlying regionalized variables (a well-known geostatistical term) are generated to facilitate error propagation in spatial analyses and applications [4,7,12]. This method is, theoretically, more rigorous than methods that assume independent and identically distributed positional errors [47–51].

Variogram-based geostatistical simulation is conventionally used for the stochastic simulation of regionalized variables, such as positional errors [52]. This is non-trivial if co-simulation for bivariate positional errors (X and Y coordinates) is to be carried out, as auto- and cross-covariance for errors in X and Y coordinates need to be modeled.

Multi-point geostatistics (MPS) is better suited for simulating regionalized variables with complex patterns and for use in various applications [53–57]. Instead of variogram models, MPS uses training images (TIs) as templates of spatial structures that are deemed representative of the problem domains. MPS produces conditional realizations honoring the high-order statistics, as opposed to traditional two-point statistics (e.g., variograms), represented in univariate or multivariate TIs. As an important technique in MPS, the direct sampling (DS) algorithm has advantages for modeling both categorical and continuous variables and is able to handle multivariate co-simulation [58]. For DS, both regularly spaced and completely informed TIs and irregularly sampled and incompletely informed training data (TD) can be used for simulation [59]. As a refinement to the conventional DS algorithm, QuickSampling (QS) [60] is advantageous in terms of the improved computational efficiency and flexibility of using TI or TD. To the best of our knowledge, MPS in general and DS in particular have rarely been pursued for positional-error modeling. This research seeks to fill this important niche.

To proceed with MPS-based simulation, there are two hurdles to overcome. One concerns the handling of non-stationarity in positional errors in images, and the other is about a cost-effective strategy for constructing TIs or TD. These issues are discussed below.

A key feature for positional errors in images is their systematic components (i.e., trends or local means). The trends are often major components, which result from image tilts or satellite attitude oscillations [61,62], terrain relief [37,40,63], or surface undulation [46,64] and are likely to be present even after initial image georectification, as discussed in [65], where image vendor-supplied sensor models in the form of rational polynomial coefficients (RPCs) were not sufficiently accurate. For images flown on different sensors and over different areas, positional errors and their trends are bound to be different (i.e., non-stationary), precluding the transferability of TD built on particular types of images over specific training areas to different areas, even when the same types of sensors/images are used. Thus, trends need to be accounted for in positional-error modeling so that de-trended errors (i.e., residuals) may become stationary in terms of spatial statistics and, thus, can be effectively used for MPS.

Trend-surface analysis may be performed using various methods, including polynomials and thin-plate smoothing splines [66–68]. In the geolocation and co-registration of satellite images [69], thin-plate splines, as special types of radial basis functions, are often used [70,71]. In this research, thin-plate splines were employed to decompose positional-error fields into trends and residuals. This points to the methodology of generalized additive modeling (GAM) [72,73], which (being a machine learning method) is a generalized linear model with a linear predictor involving a sum of smooth functions, including thin-plate smoothing splines. GAM was well-suited for this research, as it can be implemented either via smoothing splines or partial splines incorporating extra explanatory variables [67].

As mentioned above, the other issue concerns TD, which need to be furnished for MPS simulation. Note that TD for residuals is required here, since de-trending of positional errors is necessary, as discussed above. Manual image digitization for densely sampled TD is time-consuming and may be feasible only for very small study sites. Relatively dense TD may be cheaply obtained by using the technique of digital-image matching [74–80], given the existence of reference images. However, this technique may not be easily used for HSR images that feature complicated urban fabrics, even when they are initially georectified, as was the case for this study. This is because the so-called orthoimages that are routinely produced are often only georectified using digital elevation models (DEMs) rather than digital surface models (DSMs) and, thus, they are not truly orthorectified images—especially those in the presence of non-terrain 3D spatial entities (e.g., buildings) [33,40,81,82]. Image displacements due to surface undulation are often complicated by image occlusions. In turn, these occlusions give rise to ambiguities and errors in the identification of homologous image points through computer image matching and, hence, errors in the derivation of accurate image displacements, not to mention other kinds of complexity, such as shadows and unwanted objects in images and the effects of temporality between the reference images and the test images.

Clearly, the combined use of automatic image correlation and visual screening (for raw displacement data cleaning) provides a feasible solution in generating relatively dense and quality-enhanced TD. Therefore, the strategy in this study was to furnish relatively dense TD by using digital-image correlation to identify homologous image points and to measure positional errors. This was followed by visually screening raw displacement data to filter out gross errors that were due to the misidentification of homologous points and the contamination of non-terrain image objects, which are common in HSR images.

The main contribution of this research lies in the novel use of MPS (DS in particular), GAM, and digital-image correlation to characterize positional errors in HSR images, where DS functions as a non-parametric and multivariate simulator for positional errors, GAM de-trends positional errors, and digital-image correction (followed by visual screening) constructs relatively dense and quality-enhanced TD. Simulated positional errors will facilitate error propagation in applications, such as the extraction of road centerlines from images. In addition, with mean errors in positions computed from error realizations, reference positions for positions of interest can be estimated through error correction, providing a method of enhanced georectification.

2. Materials and Methods

The flowchart for this research on positional-error characterization is shown in Figure 1, in which a set of homologous image points are manually digitized, with errors in the X and Y coordinates calculated, resulting in reference sample data, from which reference values of positional errors were derived. The reference dataset consisted of a reference sample of 581 points (for model training in GAM and as CD in MPS) and a test sample of 60 points. Image correlation was applied to generate relatively dense raw measurements of positional errors (i.e., raw displacements), which were then screened to filter out erroneous points, resulting in quality-enhanced displacement data, a subset of which were used as TD in this research. GAM was used to extract trend surfaces and, thus, residuals for both CD and TD. Using de-trended TD and CD, realizations of residuals and, hence, positional errors were generated at a grid of 80 m resolution. The metrics of positional errors (i.e., means, standard deviation, and cross-correlation) were then generated by summarizing these positional-error realizations. Realizations of errors along road centerlines (RCLs) were obtained by interpolation over the aforementioned error surfaces that were simulated, while the error metrics for RCLs could be computed and recorded as extra line attributes. Mean reference positions for RCLs could also be estimated from their digitized versions on the test image and from positional errors derived from DS simulation through error correction. Using test sample data, the simulated reference RCLs could be assessed with respect to their accuracy. A further description of these methods is provided below.

2.1. The Study Area and Datasets

This research was based in the Shanghai municipality, China. Shanghai is a major coastal city, being China’s commercial, financial, industrial, and trading center. Its terrain undulation is modest, suggesting little impact of terrain relief therein on image displacements. A square area of 40 km by 40 km was chosen as the study site, as shown in Figure 2.

A georectified image subset (panchromatic) of 0.5 m spatial resolution, flown during the summer in 2020, was used as the reference image, as shown in Figure 2a. A ZY-3 satellite image subset (panchromatic band), acquired on 21 February 2020 and resampled to 2.0 m resolution, was used as the experiment test image (often known as the target image or the sensed image in relevant literature), as shown in Figure 2b. The images were initially georectified and radiometrically corrected, being part of the data sources for building up the generalization point cloud dataset described in [32].

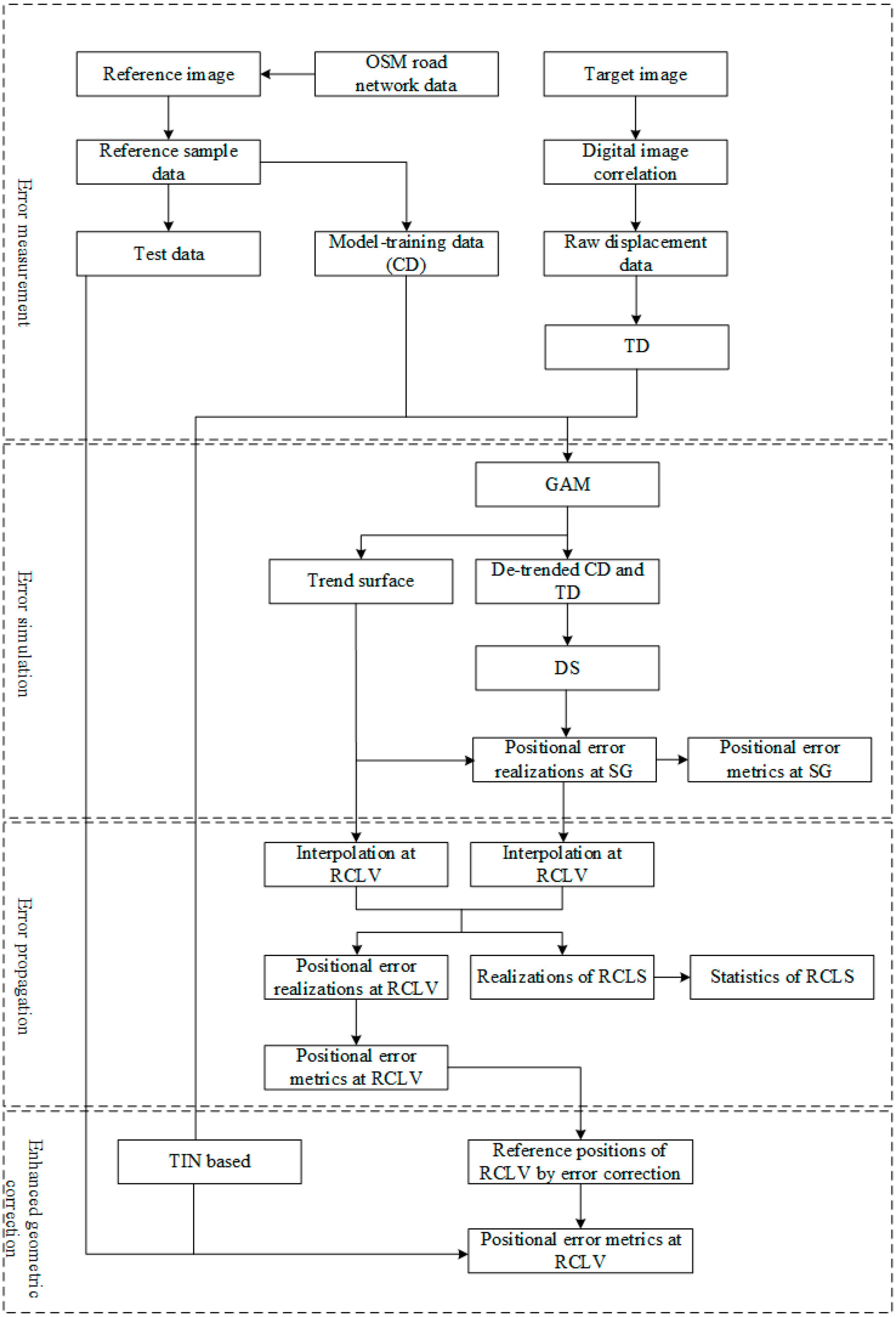

Figure 1. The flowchart for characterizing positional errors, where OSM stands for OpenStreetMap, SG represents simulation grid nodes, RCLV represents road centerline vertices, and RCLS represents road centerline segments.

A total of 641 homologous image points were visually located and digitized on the reference-test image pair, 581 of which (shown as green dots in Figure 2a) were used as CD in MPS and also for model training in GAM and variogram modeling, while 60 of which (shown as red dots in Figure 2b) were used as test sample data. The model-training sample pixels seemed to be regularly distributed, as shown in Figure 2a. In fact, they were only approximately so. In principle, any well-defined image pixels can be candidates for training pixels. However, our preliminary tests revealed that irregularly distributed training pixels were advantageous for effectively de-trending positional errors to enhance stationarity in resultant residuals, thereby facilitating effective DS-based simulation through constructing TD from a sub-area rather than the whole study area. Major roads are also depicted in Figure 2b; they are are used to illustrate error propagation and positional-error correction. For ensuring accuracy in the reference sample data (of positional errors), centers of low houses (mostly in the rural areas), centers of landmarks, and road intersections were measured, by referring to the generalized point cloud dataset [32] and OSM road network data. Note that the use of the generalized point cloud dataset was limited, in the sense that only browsing was permitted, due to its being considered as classified data at this stage.

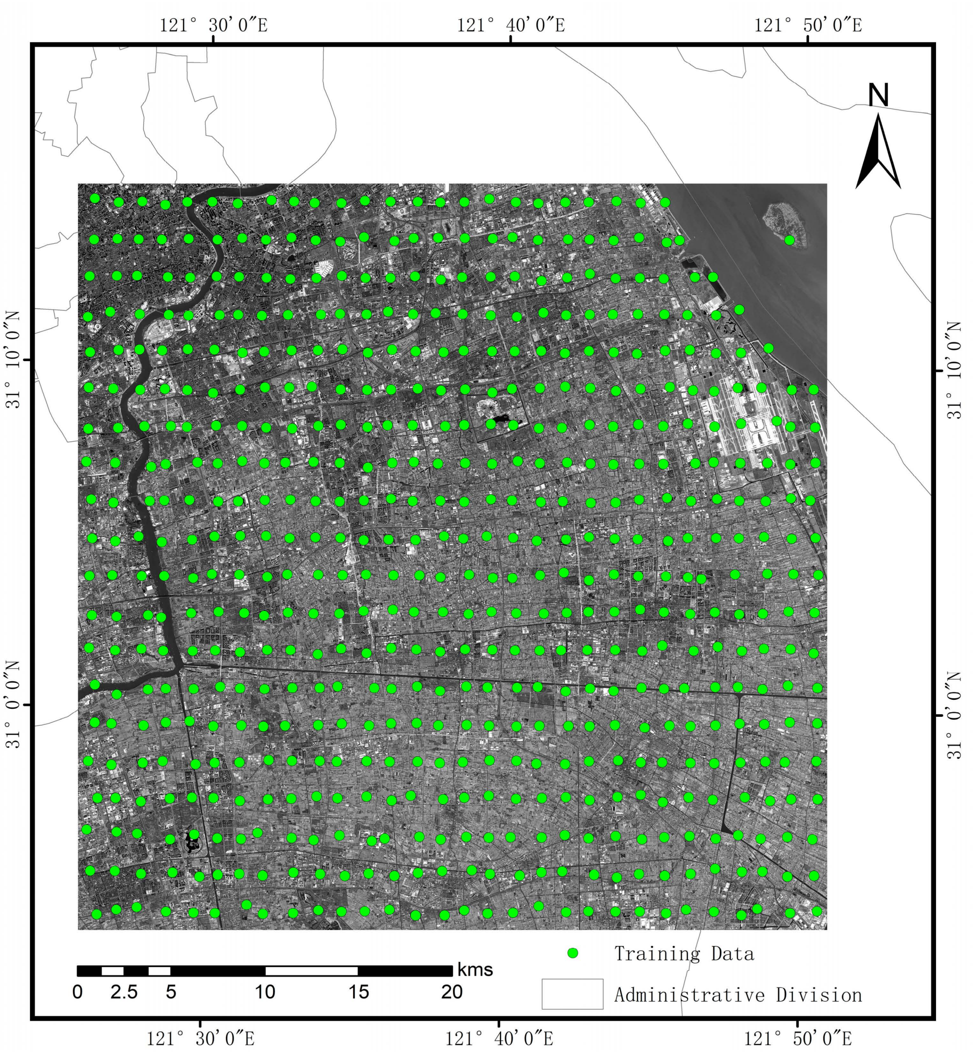

(**a**)

Figure 2. *Cont.*

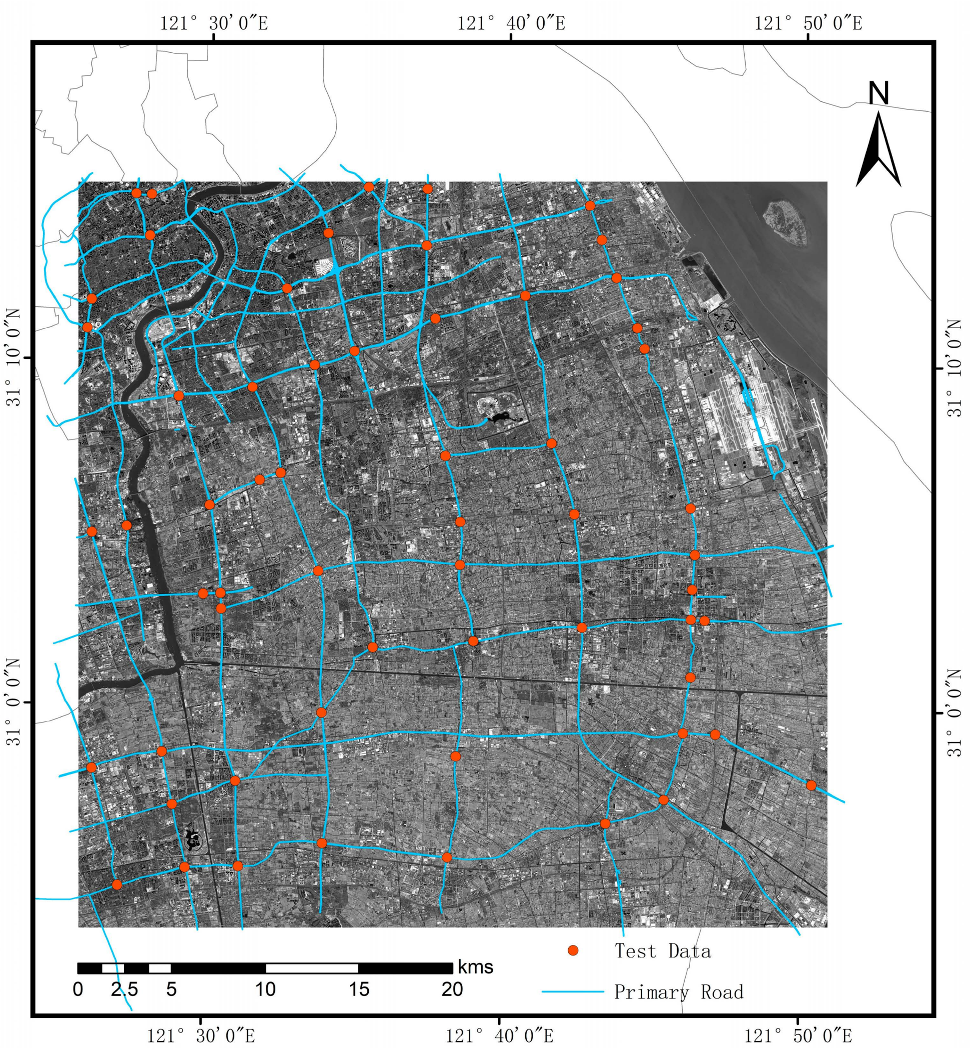

(**b**)

Figure 2. The reference-test image pair in this research: (**a**) the reference image with green dots indicating model-training sample points and (**b**) the test image in which road centerlines are shown as blue lines and test sample points are shown as red dots.

The means and the standard deviation for positional errors in the X and Y coordinates in the experiment reference-test image pairs are reported in Table 1; they were estimated based on the model-training data (i.e., the CD) and the test sample data, respectively. As indicated in Table 1, the metrics of positional errors were mostly similar between those of the training sample data and the test sample data, except for the minimum error in X and the standard deviation in Y

Table 1. Summary of positional errors evaluated by the reference sample data (m).

	Min	**Max**	**Mean**	**Standard Deviation**
Model-training data_X	−3.43	2.33	−0.05	0.75
Model-training data_Y	−5.40	5.59	−0.78	0.99
Test sample data_X	−2.49	2.23	−0.10	0.86
Test sample data_Y	−5.64	5.29	−1.08	1.48

2.2. Semi-Automatic Construction of TD

As described in the Introduction, a combination of image correlation (for collecting raw displacement data) and visual screening provided a feasible solution for obtaining relatively dense and reliable TD for MPS.

By digital image correlation, homologous image points in a reference-test image pair were identified using image-matching algorithms, for which a formula for matching cost is provided in the Appendix A. This allowed for the differences between the reference image and the test image (i.e., displacements or positional errors of points in the test image relative to the assumed reference image) to be estimated automatically. The software package MicMac (version 1.0. beta14) [78] was used for automatically measuring displacements of features on the test image with respect to the reference image.

To filter out gross errors in the aforementioned raw displacement data, it was necessary to select well-defined, easy-to-locate, visible (on both reference and test images), and ground-level entities that were free of gross errors that were due to surface undulation displacements, image point mismatches, and other artifacts. This implied that image segments over water bodies, building sides, wooded land, shadows, and other areas of uncertainty needed to be masked out. This process was assisted in this study by using the generalized point cloud dataset [32] and OSM road network data with the understanding that road surfaces visible on images were not subject to displacements due to terrain relief when the experiment images were initially georectified.

2.3. GAM for De-Trending Positional Errors

As mentioned in the Introduction, systematic components are usually present and often of major proportion in positional errors, even if they are initially georectified. We needed to de-trend positional errors (for both TD and CD) as a way to handle non-stationarity [54,56] for geostatistical simulation-based error modeling.

For this research, the R-package Mixed GAM Computation Vehicle with Automatic Smoothness Estimation (MGCV) [73] was used for GAM-based trend-surfacing in CD and TD. In MGCV, GAMs (in particular, thin-plate splines) attempt to find the appropriate smoothness for each applicable model term, using prediction-error criteria or likelihood-based methods. The prediction-error criteria used are those of generalized cross validation (GCV) when the scale parameter is unknown. Clearly, GAM estimates the degree of smoothness as part of model fitting [72]. In the Appendix A, thin-plate splines are described.

With GAMs fitted to the data, trend surfaces were predicted over the study area and over the extent of the TD, respectively. Then, residuals were computed at locations of CD and TD, accordingly. De-trended CD and TD were used in DS, as discussed below.

2.4. DS for Simulating Positional Errors

DS was used to simulate a large number of equal-probable residual simulations (and then positional errors). DS is a conceptually simple, yet functionally powerful, MPS algorithm, as it directly samples the TD for a given data event instead of counting and storing the configurations found in Tis, as in some other MPS algorithms [53].

DS proceeds as follows. Starting from an initial randomly located point along a chosen random path, the TD are scanned. For each of the successive sampling window, the mismatch metric (distance metric) between the data event informed in the SG and the mismatch metric sampled from the TD are calculated. If the mismatch is lower than a given threshold, the sampling process is stopped and the value at the central node of the data event in the TD is directly taken as the simulated value at the SG node under consideration [58,59]. The mismatch metrics used in DS are described in the Appendix A.

An MPS framework, G2S [60], was used in this research. We applied a resolution of 80 m for gridding TD and for specifying SG nodes. In this way, matching between data events in TD and SG, with a geometric tolerance of 40 m, was implicitly enforced. DS was run using the multivariate approach, as positional errors are bivariate (with X and Y coordinates). Equal weighting was applied to the X and Y coordinates.

The simulated error surfaces (100 surfaces) were summarized per individual SG nodes as maps of means, standard deviation, and covariance (between X and Y) of residuals. The estimated trend surface estimated was added to the mean residuals to obtain a surface of mean positional errors, while the maps of standard deviation and X–Y covariance in positional errors were equal to those of residuals.

It is useful to view these surfaces of positional-error metrics as imaginary fields of corresponding quantities over the image domains—even over image segments in which the objects of interest are not visible, as is often the case with HSR images of urban scenes. This is because images are often not truly orthorectified, as explained in Section 1.

2.5. Positional-Error Propagation in Road Centerlines

In this research, error propagation aimed to simulate errors at vertices defining a set of RCLs that was chosen for experiments. With a number of equal-probable realizations of residuals simulated, as described in Section 2.4, it was possible to obtain realizations of positional-error residuals at RCL vertices (RCLVs, as shown in Figure 1) by interpolation, as an approximate approach (a theoretically rigorous way would be simulation at RCLVs directly). The simulations at RCLVs could then be summarized to obtain the metrics of the residuals of the positional errors therein.

For simulating positional errors at RCLVs, we estimated trend values of positional errors at the vertices by interpolating on the trend surfaces estimated separately (see Section 2.3). Positional-error realizations at the vertices were obtained by adding the estimated trend-surface values to residual realizations. The mean positional errors were the sum of mean residuals and trend-surface values, while the standard deviation and the X-Y covariance at individual vertices remained the same as those in the residuals.

RCLs were then simulated. In addition, the lengths of some of the RCL segments were summarized in terms of means and standard deviation.

2.6. Realizations of References Positions for Road Centerlines

As described in Section 2.5, positional errors at SG nodes and RCLVs can be simulated in a large number of equal-probable realizations. Simulated positional errors can also be used to simulate reference positions of points of interest. This amounts, effectively, to enhanced georectification.

For this purpose, we performed georectification to some of the selected RCL segments, where reference data were available (so that accuracy gains could be evaluated) over the test image, through error correction. Alternatively, using CD as control data, we also performed image rectification to the test image, based on the triangulated irregular network (TIN).

3. Results

3.1. Constructing TD

MicMac (through its interface MM2DPosSism) was used to identify homologous image points and to generate full-coverage raw displacement data for constructing TD. To ensure accuracy in image-correlation-derived displacement data, they were visually filtered, with the generalized point cloud dataset [32] and the OSM road data layer used as a guide, as described in Section 2.2. A subset image of raw displacements of 10 km by 10 km in the center of the study area was selected for constructing TD at 80 m resolution. Well-defined image points were kept, while image segments over water bodies, building sides, wooded land, shadows, and other areas of uncertainty were removed.

The image-correlation-derived displacement data before and after filtering were assessed, as shown in Table 2, in which the means and the standard deviation of displacement data are very close before and after filtering, with outstanding differences in minimum and maximum values. This was unsurprising, given the fact that filtering was only applied to apparently mis-matched image points.

Table 2. Summary statistics of displacement data before and after filtering (m).

	Min	Max	Mean	Standard Deviation
displacement_X	−4.63	2.62	−1.04	0.46
displacement_Y	−7.01	3.15	−1.92	0.86
filtered displacement_X	−4.0	1.54	−1.05	0.43
filtered displacement_Y	−4.0	1.40	−1.92	0.73

3.2. Trend-Surfacing CD and TD

For trend-surfacing the CD and the TD, GAM in the R-package MGCV was applied, using splines as smoothers. Smooth functions of image points' positions were used, with displacements being incorporated as covariates in the case of TD. Smoothness was determined, along with model parameters, based on the criterion of GCV. The results are shown in Table 3, indicating that GCV scores were similar for modeling fitting over the domains of CD and TD.

Table 3. GCV results for GAM-based trend-surface analysis of CD and TD (m).

	GCV_X	GCV_Y
CD (smoothing splines)	0.52	0.92
TD (smoothing splines + displacements)	0.49	0.81

The residuals after GAM-based trend surfacing were also used to calculate experimental auto- and cross-variograms. Then, they were fitted with theoretical variogram models, as shown in Table 4.

Table 4. Auto- and cross-variogram models for de-trended positional errors in X and Y coordinates.

	Variogram Model
Auto-variogram in X	0.3148 × Nugget + 0.17428 × Stable (1911.2,2)
Auto-variogram in Y	0.4671 × Nugget + 0.48685 × Stable (5248.5,0.63418)
Cross-variogram between X and Y	0.33837*Nugget + 0.14993*Stable (2019.5,2)

3.3. Simulating Positional Errors

With de-trended CD and TD, DS-based MPS was carried out. A resolution of 80 m was chosen, since the objective of this research was to characterize positional errors in selected roads rather than individual pixels of the images involved. Another reason was that geostatistical simulation over a large municipality at a fine resolution, such as that of the original image resolution, would have been prohibitively expensive, computationally. The simulated positional-error surfaces, which represented the sums of residual realizations (100 in total) and trend-surface values at SG nodes, were summarized to derive means, standard deviation, and covariance between errors in the X and Y coordinates at the SG nodes (80 m resolution). They are shown in Figure 3, where Figure 3a,b show the means of positional errors in X and Y, respectively, Figure 3c,d depict the standard deviation in X and Y, respectively, while Figure 3e shows the covariance of errors in X and Y.

For comparison, sequential Gaussian simulation (SGSIM) was also used to simulate positional errors, based on the variogram models in Table 4. To simplify the matter and, given that the focus of this research was on the combined use of MPS, GAM, and image correlation for error modeling, the positional errors in X and Y were simulated separately by SGSIM, meaning that no attempts were made at joint simulation of errors in X and Y using a linear model of co-regionalization.

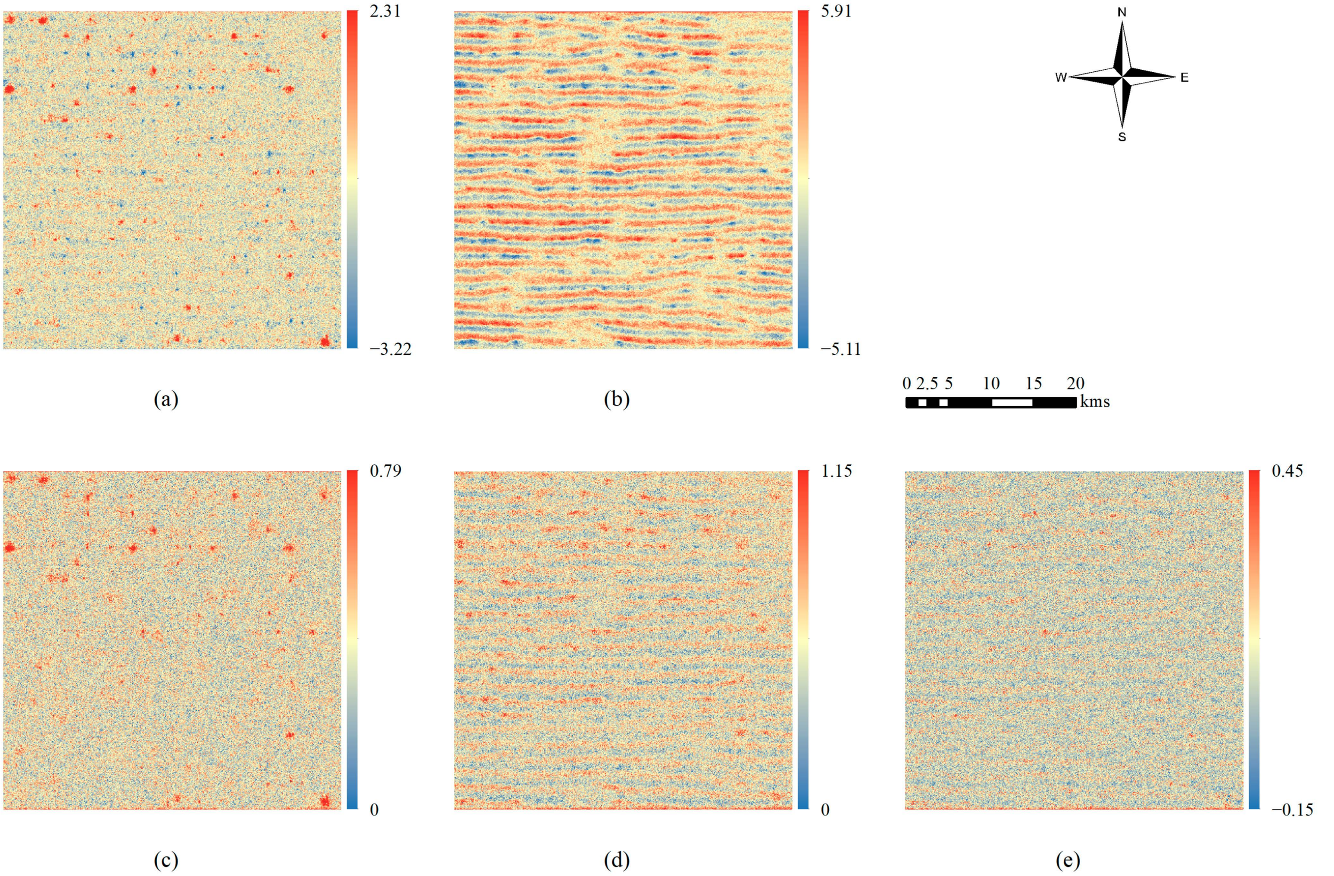

Figure 3. Positional errors characterized through MPS: (**a**,**b**) show means in X and Y, respectively, and (**c**,**d**) show standard deviation in X and Y, respectively, and (**e**) shows covariance of errors in X and Y.

3.4. Characterizing Errors in Road Centerlines and Predicting Their Reference Positions

Equal-probable realizations of positional errors in selected RCLVs were approximated by interpolation of both DS-simulated residuals and trend-surface values at the RCLVs and totaling them, as illustrated in Figure 1 and described in Section 2.5. The error metrics estimated via simulation were recorded as extra attributes to the selected RCLs. The means and standard deviation in the lengths of the seven selected RCL segments were summarized, based on 100 realized RCLs. The results are shown in Table 5, in which reference values of the lengths of the seven RCL segments (which were calculated based on the test sample data consisting of reference positions of RCLVs related to the seven RCL segments) are also shown, along with the means and standard deviation obtained from DS-simulated RCL segments. As indicated in Table 5, the differences between the mean lengths of all seven RCL segments and their reference values were within tiny fractions of their standard deviation, suggesting small errors in the lengths, due to spatial correlation in positional errors, as expected.

Table 5. Means and standard deviation in length of some of RCL segments, derived from DS simulation (m).

Selected RCL Segments	Reference Values	Means	Standard Deviation
1	1605.15	1605.07	1.08
2	729.47	729.45	0.51
3	3092.66	3092.57	1.23
4	5839.37	5839.49	0.50
5	3597.71	3597.57	0.69
6	3450.23	3450.49	1.02
7	2878.63	2878.85	1.06

Reference positions of the selected RCLs were estimated through error correction, based on location-specific mean positional errors derived from simulation. Alternatively, the georectification of RCLs was also carried out, using a TIN-based correction method, with the same reference sample of 581 points used as control data. The estimated reference positions for the selected RCLs, through error corrections using location-specific positional errors estimated by TIN, SGSIM simulations, and DS simulations, were assessed with respect to accuracy against the test sample of 60 points. The results are shown in Table 6. As indicated in Table 6, TIN's performance was only slightly inferior to those of SGSIM and DS, except by the criterion of maximum absolute error (MAE), while the performances of DS and SGSIM in terms of mean error (ME), MAE, and root mean squared error (RMSE) were very comparable.

Table 6. Comparisons of georectification by positional-error corrections based on TIN, SGSIM, and DS (m).

	ME	**MAE**	**RMSE**
TIN_X	0.10	0.38	0.96
TIN_Y	−0.81	0.91	1.61
SGSIM_X	0.02	0.66	0.89
SGSIM_Y	−0.74	0.96	1.57
DS_X	0.10	0.69	0.91
DS_Y	−0.72	0.91	1.48

Further explanations of the largely similar performances of TIN, SGSIM, and DS were based on the interpretation of variogram models shown in Table 4. Based on the definitions of the stable model of variograms, the effective ranges of spatial correlation were calculated as 3310.3 m and 3498.0 m in X and Y, respectively. This indicated that the sampling interval should have been at an average of about 1655.1 m and 1749.0 m in X and Y, respectively, according to the sampling theorem versed in terms of the range parameter in variogram models [83]. The average sampling intervals in X and Y were about 1333.3 m and 2000.0 m in X and Y, respectively, suggesting sufficiency in sampling for X and slight undersampling in Y. Thus, theoretically, it is not surprising that the accuracy of enhanced georectification of the test image by different methods was very comparable, given a largely adequate sampling density of reference sample data over the study area. However, the advantages of DS over SGSIM and TIN were likely more manifested in the case of small-sized reference sample data, whereas DS capitalized on using TD that were cheaply generated from computer-image correlation, as demonstrated in this research.

4. Discussion

4.1. Summary of the Work

The methods proposed in this study address some of the challenging issues pertaining to positional-error modeling in remote-sensing images of HSR: non-parametric and joint simulation of positional errors in X and Y coordinates, non-stationarity in-positional errors, and construction of TD for geostatistical simulation. The contribution of the proposed method lies in the following factors: multivariate MPS for non-parametric and joint simulation of bivariate X–Y positional errors (as opposed to a conventional variogram based two-point geostatistical simulation [52]), GAM to de-trend positional errors to handle non-stationarity in-positional errors, and digital-image correlation to furnish TD efficiently.

These approaches have potential for various applications. For instance, they are valuable for the analysis of the effects of positional errors (e.g., misregistration) upon image classification, change detection, creation of DEMs, species-distribution modeling, and spatial ecology, wherein positional errors should be properly accounted for [84–89]. The proposed methods will also be beneficial for the fusion of multi-source data, wherein differences in bias and variance of positional errors in the datasets that are being fused need to be properly accounted for.

4.2. Further Research

In the future, while it is important to improve computing efficiency of the DS algorithm [60], especially when simulations at finer resolution and/or over larger areas are required, there is a pressing need to advance methods for TD construction [56], especially for simulations at fine resolution and over heterogeneous areas. It is worth exploring how we may benefit from the complementary use of DS and SGSIM (and other variogram-based geostatistical simulators). For instance, they may be used co-operatively in a multigrid framework [55]—using DS to generate simulations at a coarser resolution while using SGSIM for fine-resolution simulations.

Trend surfacing may also be addressed by random forest (RF), another machine learning approach. In a separate experiment, not reported here, RF was applied over smaller subset images, with image points' positions and image textures used as explanatory variables. The results were found to contain artifacts of image textures, although GCV scores were found to be comparable to those of GAM.

Note that reference images may themselves be subject to errors, especially when they are not truly orthorectified, due to the existence of non-terrain height objects, while image occlusions will further complicate image correlation (and, hence, TD construction) and error modeling. This was exactly the case with the experiment images used in this study, in which visual screening was necessarily undertaken to remove gross errors in raw displacement data that were generated automatically through MicMac-based image correlation. This points to the relevance of true digital orthoimage maps (TDOMs) for further research.

For the production of TDOMs, in which image displacements are corrected not only for image tilts and terrain relief, but also for surface undulation, we need to have DSMs, in addition to image orientation and DEMs, to correct image displacements pertaining to non-terrain entities (e.g., buildings and trees). DSM creation remains an issue, despite developments in photogrammetric processing and LiDAR for generating DSMs. We also need to improve methods for handling occlusions that are common in urban scenes. The creation of TDOMs will certainly benefit from the establishment of the generalized point cloud dataset mentioned previously [32], and vice versa.

TDOMs and the fully functioning of the generalized point clouds [32] would allow us to pursue integrated error modeling and geographic-information processing. We would be able to describe and model horizontal and vertical dimensions of errors in DEMs. More importantly, in an integrated framework, TDOMs, DSMs, DEMs, digital line graphs (DLGs), and other data layers (e.g., [90]) can be jointly analyzed with respect to errors. This would allow for the rigorous georectification of objects and for the proper geocoding of images and geo-fields, and in turn provide for the unifying framework of all information layers concerned.

Ultimately, it would be possible to address the issue of geospatial-information fusion with uncertainty accounted for, as hinted at in Section 4.1. For example, object detection would be enhanced, with consideration for positional and thematic uncertainty. Temporal inconsistency would be analyzed in relation to change detection in land use and land cover, elevation, and other types of information layers. Information about 3D structures would be analyzed, such as that related to buildings and trees.

5. Conclusions

This research contributes to positional-error characterization in remote-sensing images of high spatial resolution (HSR) using a combination of multi-point geostatistics (MPS), machine learning, and digital-image correlation methods. Specifically, direct sampling (DS) was used to facilitate non-parametric and joint simulation-based modeling of bivariate positional errors in X and Y coordinates; generalized additive models (GAMs) using spline smoothers were employed to decompose positional errors into systematic and random but spatially correlated components to handle non-stationarity errors; and image correlation based on MicMac, followed by visual screening, was used as a cost-effective means for the extraction and construction of training data (TD) for MPS.

Experiments based on the Shanghai municipality in China confirmed the effectiveness of the proposed methods for modeling positional errors in HSR images. The proposed methods were developed in the context of initially orthorectified images, with the image of finer resolution used as reference. However, the proposed methods are applicable for use in the context of reference-test image pairs of coarser resolutions, images with or without initial orthorectification, and reference maps (instead of reference images). More importantly, the proposed methods will be valuable not only for positional-error modeling and geometric aspects in images, such as image rectification and co-registration, but also for integrated information processing, where positional errors need to be factored in.

Author Contributions: Conceptualization, L.X., W.Z. and J.Z.; data curation, L.X., J.W. and S.W.; formal analysis, W.Z. and J.W.; funding acquisition, L.X.; investigation, W.Z. and J.W.; methodology, L.X., W.Z., J.W. and J.Z.; project administration, L.X. and S.W.; resources, L.X.; Software, W.Z., J.W. and J.Z.; supervision, J.Z.; validation, L.X., J.W. and S.W.; visualization, W.Z. and J.W.; writing—original draft, L.X., W.Z., J.W. and J.Z.; writing—review & editing, L.X., W.Z. and J.Z. All authors have read and agreed to the published version of the manuscript.

Funding: This research was funded by the Shanghai Surveying and Mapping Institute through a grant for the development of generalized point clouds and China's Natural Science Foundation (grant no 41471375).

Acknowledgments: Mariethoz and Mathieu from the University of Lausanne, Switzerland, provided help in using QuickSampling (QS). Luc Girod from the University of Oslo, Norway, kindly offered advice on using MicMac.

Conflicts of Interest: The authors declare no conflict of interest.

Appendix A

Appendix A.1. Multi-View Stereo Image Matching in MicMac

In MicMac, the matching cost function can be expressed as [78]

$$\varepsilon(F_{px}) = \iint_T A(x, y, F_{px}(x, y)) + \|\nabla F_{px}\|^{reg} \tag{A1}$$

where $\|\nabla F_{px}\|^{reg} = \alpha_1 * \left|\nabla F_{px}^1\right| + \alpha_2 * \left|\nabla F_{px}^2\right|$, $A(x, y, F_{px}(x, y))$ is the measure of similarity between pixels ($A(x, y, F_{px}(x, y)) = 0$ when identical), $\|\nabla F_{px}\|^{reg}$ is a norm of the gradient and used for regularization, and α_1, α_2 are regularizations on the first and second component. The measurement of similarity can be computed from the normalization cross-correlation coefficient (*corr*) via $1 - corr$.

Appendix A.2. Thin-Plate Spline Smooth in GAMs

The generalized additive models extend standard linear models by replacing variables with smooth functions. The model can be written as

$$y_i = \beta_0 + \sum_{j=1}^{p} f_j(x_{ij}) + \epsilon_i \tag{A2}$$

where f_j is the smooth function of the jth predictor. In this study, thin-plate spline was chosen as the smooth function and can be expressed as

$$\hat{f}(\mathbf{x}) = \beta_0 + \boldsymbol{\beta}^T \mathbf{x} + \sum_{j=1}^{N} \alpha_j h_j(\mathbf{x}) \tag{A3}$$

where $\mathbf{x} = (x, y)^T$ is the positional coordinates, α represents the coefficients of warping subject to N control points, and $h_j(\mathbf{x}) = \|\boldsymbol{x} - \mathbf{x}_j\|^2 log\|\boldsymbol{x} - \mathbf{x}_j\|$ is the radial basis function for thin-plate splines.

Appendix A.3. Mismatch Metrics of DS/QS

In MPS algorithms, a data event is defined as a data point at and around a target location $\mathbf{x}$ and is expressed as

$$dev(\mathbf{x}) \equiv \{(\mathbf{h}, \mathbf{Z}(\mathbf{x} + \mathbf{h})), \mathbf{h} \in N(\mathbf{x})\} \tag{A4}$$

where $\mathbf{h}$ is the lag vector, $N(\mathbf{x})$ is the defined neighbor, and $\mathbf{Z}(\mathbf{x} + \mathbf{h})$ is the multivariable vector at location $\mathbf{x} + \mathbf{h}$. The simplest distance between univariate data event $dev(\mathbf{x}_1)$ and $dev(\mathbf{x}_2)$ is

$$d(dev(\mathbf{x}_1), dev(\mathbf{x}_2)) = \frac{1}{n}\sum_{i=1}^{n}|Z(\mathbf{x}_1 + \mathbf{h}_{\boldsymbol{i}}) - Z(\mathbf{x}_2 + \mathbf{h}_{\boldsymbol{i}})|^p \tag{A5}$$

where p is an exponent. The distance corresponds to the Euclidean distance when $p = 2$ and corresponds to the Manhattan distance when $p = 1$. For multivariate simulation, the mismatch metric—the distance between data events in TD/TI and SG—can be decomposed and expressed as [60]

$$d(\boldsymbol{a}, \boldsymbol{b}) \propto \sum_{i \in I}\sum_{j \in J_i} f_j(a_i) g_j(b_i) \tag{A6}$$

where $\boldsymbol{a} = (a_1, a_2, \ldots, a_I)^T$ and $\boldsymbol{b}= (b_1, b_2, \ldots, b_I)^T$ are the data event vectors, f_j and g_j are metric-depended functions, and J_i is the metric of ith variable.

References

1. Arbia, G.; Griffith, D.A.; Haining, R.P. Spatial Error Propagation When Computing Linear Combinations of Spectral Bands: The Case of Vegetation Indices. *Environ. Ecol. Stat.* **2003**, *10*, 375–396. [CrossRef]
2. Bastin, L.; Cornford, D.; Jones, R.; Heuvelink, G.B.M.; Pebesma, E.; Stasch, C.; Nativi, S.; Mazzetti, P.; Williams, M. Managing Uncertainty in Integrated Environmental Modelling: The UncertWeb Framework. *Environ. Model. Softw.* **2013**, *39*, 116–134. [CrossRef]
3. Biljecki, F.; Heuvelink, G.B.M.; Ledoux, H.; Stoter, J. Propagation of Positional Error in 3D GIS: Estimation of the Solar Irradiation of Building Roofs. *Int. J. Geogr. Inf. Sci.* **2015**, *29*, 2269–2294. [CrossRef]
4. Brown, J.D.; Heuvelink, G.B.M. The Data Uncertainty Engine (DUE): A Software Tool for Assessing and Simulating Uncertain Environmental Variables. *Comput. Geosci.* **2007**, *33*, 172–190. [CrossRef]
5. Burnicki, A.C.; Brown, D.G.; Goovaerts, P. Simulating Error Propagation in Land-Cover Change Analysis: The Implications of Temporal Dependence. *Comput. Environ. Urban Syst.* **2007**, *31*, 282–302. [CrossRef]
6. Goodchild, M.F. Spatial Accuracy 2.0. In Proceedings of the Spatial Uncertainty: Proceedings of the eighth International Symposium on Spatial Accuracy Assessment in Natural Resources and Environmental Sciences, Shanghai, China, 25–27 June 2008; pp. 1–7.
7. Goovaerts, P. Geostatistical Modelling of Uncertainty in Soil Science. *Geoderma* **2001**, *103*, 3–26. [CrossRef]
8. Li, D.; Zhang, J.; Wu, H. Spatial Data Quality and Beyond. *Int. J. Geogr. Inf. Sci.* **2012**, *26*, 2277–2290. [CrossRef]
9. Shi, W.; Cheung, C.K.; Zhu, C. Modelling Error Propagation in Vector-Based Buffer Analysis. *Int. J. Geogr. Inf. Sci.* **2003**, *17*, 251–271. [CrossRef]
10. Zhang, J.; Goodchild, M.F. *Uncertainty in Geographical Information*, 1st ed.; CRC Press: London, UK, 2002.
11. Chrisman, N.R.; Yandell, B.S. Effects of Point Error on Area Calculations: A Statistical Model. *Surv. Mapp.* **1988**, *48*, 241–246.
12. De Bruin, S.; Heuvelink, G.B.M.; Brown, J.D. Propagation of Positional Measurement Errors to Agricultural Field Boundaries and Associated Costs. *Comput. Electron. Agric.* **2008**, *63*, 245–256. [CrossRef]
13. Delafontaine, M.; Nolf, G.; van de Weghe, N.; Antrop, M.; de Maeyer, P. Assessment of Sliver Polygons in Geographical Vector Data. *Int. J. Geogr. Inf. Sci.* **2009**, *23*, 719–735. [CrossRef]
14. Gil de la Vega, P.; Ariza-López, F.J.; Mozas-Calvache, A.T. Models for Positional Accuracy Assessment of Linear Features: 2D and 3D Cases. *Surv. Rev.* **2016**, *48*, 347–360. [CrossRef]
15. Guo, Q.; Liu, Y.; Wieczorek, J. Georeferencing Locality Descriptions and Computing Associated Uncertainty Using a Probabilistic Approach. *Int. J. Geogr. Inf. Sci.* **2008**, *22*, 1067–1090. [CrossRef]
16. Zimmerman, D.; Fang, X.; Mazumdar, S.; Rushton, G. Modeling the Probability Distribution of Positional Errors Incurred by Residential Address Geocoding. *Int. J. Health Geogr.* **2007**, *6*, 1. [CrossRef]

17. Kharchenko, S.V.; Kazakov, S.G. The Experiment on Assessment of Point Position Accuracy at the Manual Digitizing of a Raster Map. *Geod. Cartogr.* **2018**, *933*, 35–45. [CrossRef]
18. Kronenfeld, B.J. Beyond the Epsilon Band: Polygonal Modeling of Gradation/Uncertainty in Area-Class Maps. *Int. J. Geogr. Inf. Sci.* **2011**, *25*, 1749–1771. [CrossRef]
19. Leung, Y.; Ma, J.-H.; Goodchild, M.F. A General Framework for Error Analysis in Measurement-Based GIS Part 4: Error Analysis in Length and Area Measurements. *J. Geogr. Syst.* **2004**, *6*, 403–428. [CrossRef]
20. Leung, Y.; Yan, J. A Locational Error Model for Spatial Features. *Int. J. Geogr. Inf. Sci.* **1998**, *12*, 607–620. [CrossRef]
21. Li, S.; Cai, H.; Kamat, V.R. Uncertainty-Aware Geospatial System for Mapping and Visualizing Underground Utilities. *Autom. Constr.* **2015**, *53*, 105–119. [CrossRef]
22. Mozas-Calvache, A.T.; Ariza-López, F.J. Detection of Systematic Displacements in Spatial Databases Using Linear Elements. *Cartogr. Geogr. Inf. Sci.* **2014**, *41*, 309–322. [CrossRef]
23. Ratcliffe, J. On the Accuracy of TIGER-Type Geocoded Address Data in Relation to Cadastral and Census Areal Units. *Int. J. Geogr. Inf. Sci.* **2001**, *15*, 473–485. [CrossRef]
24. Seo, S.; O'Hara, C.G. Quality Assessment of Linear Data. *Int. J. Geogr. Inf. Sci.* **2009**, *23*, 1503–1525. [CrossRef]
25. Tong, X.; Sun, T.; Fan, J.; Goodchild, M.F.; Shi, W. A Statistical Simulation Model for Positional Error of Line Features in Geographic Information Systems (GIS). *Int. J. Appl. Earth Obs. Geoinf.* **2013**, *21*, 136–148. [CrossRef]
26. Wernette, P.; Shortridge, A.; Lusch, D.P.; Arbogast, A.F. Accounting for Positional Uncertainty in Historical Shoreline Change Analysis without Ground Reference Information. *Int. J. Remote Sens.* **2017**, *38*, 3906–3922. [CrossRef]
27. Xavier, E.M.A.; Ariza-López, F.J.; Ureña-Cámara, M.A. A Survey of Measures and Methods for Matching Geospatial Vector Datasets. *ACM Comput. Surv.* **2016**, *49*, 1–34. [CrossRef]
28. Zandbergen, P.A. Influence of Street Reference Data on Geocoding Quality. *Geocarto Int.* **2011**, *26*, 35–47. [CrossRef]
29. Zelasco, J.F.; Donayo, J. Effectiveness of Geometric Quality Control Using a Distance Evaluation Method. *Int. J. Image Data Fusion* **2019**, *10*, 263–279. [CrossRef]
30. Zhang, W.; Leung, Y.; Ma, J. Analysis of Positional Uncertainty of Road Networks in Volunteered Geographic Information with a Statistically Defined Buffer-Zone Method. *Int. J. Geogr. Inf. Sci.* **2019**, *33*, 1807–1828. [CrossRef]
31. van Zoest, V.; van Buul, J.; Osei, F.; Stein, A. A Note on the Propagation of Positional Uncertainty in Environmental Models. *Trans. GIS* **2021**, *25*, 3119–3131. [CrossRef]
32. Liu, C.; Jia, S.; Wu, H.; Huang, W.; Zheng, N.; Akram, A. Scene Cognition Pattern of Point Cloud-Generalization Point Cloud. *Cehui Xuebao/Acta Geod. Cartogr. Sin.* **2022**, *51*, 556–567.
33. Aguilar, M.A.; del Saldaña, M.; Aguilar, F.J. Assessing Geometric Accuracy of the Orthorectification Process from GeoEye-1 and WorldView-2 Panchromatic Images. *Int. J. Appl. Earth Obs. Geoinf.* **2013**, *21*, 427–435. [CrossRef]
34. Bicheron, P.; Amberg, V.; Bourg, L.; Petit, D.; Huc, M.; Miras, B.; Brockmann, C.; Hagolle, O.; Delwart, S.; Ranera, F.; et al. Geolocation Assessment of MERIS GlobCover Orthorectified Products. *IEEE Trans. Geosci. Remote Sens.* **2011**, *49*, 2972–2982. [CrossRef]
35. Han, Y.; Oh, J. Automated Geo/Co-Registration of Multi-Temporal Very-High-Resolution Imagery. *Sensors* **2018**, *18*, 1599. [CrossRef]
36. Jeong, J.; Yang, C.; Kim, T. Geo-Positioning Accuracy Using Multiple-Satellite Images: IKONOS, QuickBird, and KOMPSAT-2 Stereo Images. *Remote Sens.* **2015**, *7*, 4549–4564. [CrossRef]
37. Loghin, A.-M.; Otepka-Schremmer, J.; Ressl, C.; Pfeifer, N. Improvement of VHR Satellite Image Geometry with High Resolution Elevation Models. *Remote Sens.* **2022**, *14*, 2303. [CrossRef]
38. Nwilo, P.C.; Okolie, C.J.; Onyegbula, J.C.; Arungwa, I.D.; Ayoade, O.Q.; Daramola, O.E.; Orji, M.J.; Maduako, I.D.; Uyo, I.I. Positional Accuracy Assessment of Historical Google Earth Imagery in Lagos State, Nigeria. *Appl. Geomat.* **2022**, *14*, 545–568. [CrossRef]
39. Pulighe, G.; Baiocchi, V.; Lupia, F. Horizontal Accuracy Assessment of Very High Resolution Google Earth Images in the City of Rome, Italy. *Int. J. Digit. Earth* **2016**, *9*, 342–362. [CrossRef]
40. Rizeei, H.M.; Pradhan, B. Urban Mapping Accuracy Enhancement in High-Rise Built-Up Areas Deployed by 3D-Orthorectification Correction from WorldView-3 and LiDAR Imageries. *Remote Sens.* **2019**, *11*, 692. [CrossRef]
41. Sánchez, M.; Cuartero, A.; Barrena, M.; Plaza, A. A New Method for Positional Accuracy Analysis in Georeferenced Satellite Images without Independent Ground Control Points. *Remote Sens.* **2020**, *12*, 4132. [CrossRef]
42. Song, A.; Kim, Y.; Han, Y. Uncertainty Analysis for Object-Based Change Detection in Very High-Resolution Satellite Images Using Deep Learning Network. *Remote Sens.* **2020**, *12*, 2345. [CrossRef]
43. Yilmaz, A.; Erdogan, M. Modelling the Orthoimage Accuracy Using DEM Accuracy and Off-Nadir Angle. *Geocarto Int.* **2020**, *35*, 1–16. [CrossRef]
44. Zhou, L.; Stein, A. Application of Random Sets to Model Uncertainty of Road Polygons Extracted from Airborne Laser Points. *Comput. Environ. Urban Syst.* **2013**, *41*, 289–298. [CrossRef]
45. Brown, K.M.; Foody, G.M.; Atkinson, P.M. Modelling Geometric and Misregistration Error in Airborne Sensor Data to Enhance Change Detection. *Int. J. Remote Sens.* **2007**, *28*, 2857–2879. [CrossRef]
46. Mundy, J.L.; Theiss, H.J. Error Propagation in Satellite Multi-Image Geometry. *IEEE Trans. Geosci. Remote Sens.* **2022**, *60*, 1–14. [CrossRef]

47. Dai, X.; Khorram, S. The Effects of Image Misregistration on the Accuracy of Remotely Sensed Change Detection. *IEEE Trans. Geosci. Remote Sens.* **1998**, *36*, 1566–1577. [CrossRef]
48. Gábor, L.; Jetz, W.; Lu, M.; Rocchini, D.; Cord, A.; Malavasi, M.; Zarzo-Arias, A.; Barták, V.; Moudrý, V. Positional Errors in Species Distribution Modelling Are Not Overcome by the Coarser Grains of Analysis. *Methods Ecol. Evol.* **2022**, *13*, 2289–2302. [CrossRef]
49. Glick, H.B.; Routh, D.; Bettigole, C.; Oliver, C.D.; Seegmiller, L.; Kuhn, C. Modeling the Effects of Horizontal Positional Error on Classification Accuracy Statistics. *Photogramm. Eng. Remote Sens.* **2016**, *82*, 789–802. [CrossRef]
50. Gu, J.; Congalton, R.G.; Pan, Y. The Impact of Positional Errors on Soft Classification Accuracy Assessment: A Simulation Analysis. *Remote Sens.* **2015**, *7*, 579–599. [CrossRef]
51. McRoberts, R.E. The Effects of Rectification and Global Positioning System Errors on Satellite Image-Based Estimates of Forest Area. *Remote Sens. Environ.* **2010**, *114*, 1710–1717. [CrossRef]
52. Zhang, J.; Kirby, R.P. A Geostatistical Approach to Modelling Positional Errors in Vector Data. *Trans. GIS* **2000**, *4*, 145–159. [CrossRef]
53. Mariethoz, G.; Caers, J. *Multiple-Point Geostatistics: Stochastic Modeling with Training Images*; Wiley-Blackwell: Hoboken, NJ, USA, 2014; ISBN 9781118662755.
54. Rasera, L.G.; Gravey, M.; Lane, S.N.; Mariethoz, G. Downscaling Images with Trends Using Multiple-Point Statistics Simulation: An Application to Digital Elevation Models. *Math. Geosci.* **2020**, *52*, 145–187. [CrossRef]
55. Straubhaar, J.; Malinverni, D. Addressing Conditioning Data in Multiple-Point Statistics Simulation Algorithms Based on a Multiple Grid Approach. *Math. Geosci.* **2014**, *46*, 187–204. [CrossRef]
56. Yin, Z.; Zuo, C.; MacKie, E.J.; Caers, J. Mapping High-Resolution Basal Topography of West Antarctica from Radar Data Using Non-Stationary Multiple-Point Geostatistics (MPS-BedMappingV1). *Geosci. Model Dev.* **2022**, *15*, 1477–1497. [CrossRef]
57. Zakeri, F.; Mariethoz, G. A Review of Geostatistical Simulation Models Applied to Satellite Remote Sensing: Methods and Applications. *Remote Sens. Environ.* **2021**, *259*, 112381. [CrossRef]
58. Mariethoz, G.; Renard, P.; Straubhaar, J. The Direct Sampling Method to Perform Multiple-Point Geostatistical Simulations. *Water Resour. Res.* **2010**, *46*, 9515170. [CrossRef]
59. Mariethoz, G.; Renard, P. Reconstruction of Incomplete Data Sets or Images Using Direct Sampling. *Math. Geosci.* **2010**, *42*, 245–268. [CrossRef]
60. Gravey, M.; Mariethoz, G. QuickSampling v1.0: A Robust and Simplified Pixel-Based Multiple-Point Simulation Approach. *Geosci. Model Dev.* **2020**, *13*, 2611–2630. [CrossRef]
61. Cao, J.; Fu, J.; Yuan, X.; Gong, J. Nonlinear Bias Compensation of ZiYuan-3 Satellite Imagery with Cubic Splines. *ISPRS J. Photogramm. Remote Sens.* **2017**, *133*, 174–185. [CrossRef]
62. Topan, H.; Oruç, M.; Taşkanat, T.; Cam, A. Combined Efficiency of RPC and DEM Accuracy on Georeferencing Accuracy of Orthoimage: Case Study with Pléiades Panchromatic Mono Image. *IEEE Geosci. Remote Sens. Lett.* **2014**, *11*, 1148–1152. [CrossRef]
63. Beekhuizen, J.; Heuvelink, G.B.M.; Biesemans, J.; Reusen, I. Effect of DEM Uncertainty on the Positional Accuracy of Airborne Imagery. *IEEE Trans. Geosci. Remote Sens.* **2011**, *49*, 1567–1577. [CrossRef]
64. Reinartz, P.; Müller, R.; Lehner, M.; Schroeder, M. Accuracy Analysis for DSM and Orthoimages Derived from SPOT HRS Stereo Data Using Direct Georeferencing. *ISPRS J. Photogramm. Remote Sens.* **2006**, *60*, 160–169. [CrossRef]
65. Shen, X.; Liu, B.; Li, Q.-Q. Correcting Bias in the Rational Polynomial Coefficients of Satellite Imagery Using Thin-Plate Smoothing Splines. *ISPRS J. Photogramm. Remote Sens.* **2017**, *125*, 125–131. [CrossRef]
66. Boer, E.P.J.; de Beurs, K.M.; Hartkamp, A.D. Kriging and Thin Plate Splines for Mapping Climate Variables. *Int. J. Appl. Earth Obs. Geoinf.* **2001**, *3*, 146–154. [CrossRef]
67. Huang, C.; Zheng, X.; Tait, A.; Dai, Y.; Yang, C.; Chen, Z.; Li, T.; Wang, Z. On Using Smoothing Spline and Residual Correction to Fuse Rain Gauge Observations and Remote Sensing Data. *J. Hydrol.* **2014**, *508*, 410–417. [CrossRef]
68. Hutchinson, M.F. Interpolating Mean Rainfall Using Thin Plate Smoothing Splines. *Int. J. Geogr. Inf. Syst.* **1995**, *9*, 385–403. [CrossRef]
69. Oldoni, L.V.; Del'Arco Sanches, I.; Picoli, M.C.A.; Rohden Prudente, V.H.; Adami, M. Geometric Accuracy Assessment and a Framework for Automatic Sub-Pixel Registration of WFI Images from CBERS-4, CBERS-4A, and Amazonia-1 Satellites over Brazil. *Remote Sens. Appl. Soc. Environ.* **2022**, *28*, 100844. [CrossRef]
70. Yan, L.; Roy, D.P. Improving Landsat Multispectral Scanner (MSS) Geolocation by Least-Squares-Adjustment Based Time-Series Co-Registration. *Remote Sens. Environ.* **2021**, *252*, 112181. [CrossRef]
71. Zitová, B.; Flusser, J. Image Registration Methods: A Survey. *Image Vis. Comput.* **2003**, *21*, 977–1000. [CrossRef]
72. Wood, S. *Generalized Additive Models: An Introduction with R*, 2nd ed.; Chapman and Hall/CRC: Boca Raton, FL, USA, 2017.
73. Wood, S. Mgcv: Mixed GAM Computation Vehicle with Automatic Smoothness Estimation. In *R Package Version*; R Foundation for Statistical Computing: Vienna, Austria, 2022.
74. Aati, S.; Milliner, C.; Avouac, J.-P. A New Approach for 2-D and 3-D Precise Measurements of Ground Deformation from Optimized Registration and Correlation of Optical Images and ICA-Based Filtering of Image Geometry Artifacts. *Remote Sens. Environ.* **2022**, *277*, 113038. [CrossRef]
75. Ayoub, F.; Leprince, S.; Avouac, J.-P. Co-Registration and Correlation of Aerial Photographs for Ground Deformation Measurements. *ISPRS J. Photogramm. Remote Sens.* **2009**, *64*, 551–560. [CrossRef]

76. Leprince, S.; Barbot, S.; Ayoub, F.; Avouac, J.-P. Automatic and Precise Orthorectification, Coregistration, and Subpixel Correlation of Satellite Images, Application to Ground Deformation Measurements. *IEEE Trans. Geosci. Remote Sens.* **2007**, *45*, 1529–1558. [CrossRef]
77. Oh, J.; Toth, C.; Grejner-Brzezinska, D. Automatic Georeferencing of Aerial Images Using Stereo High-Resolution Satellite Images. *Photogramm. Eng. Remote Sens.* **2011**, *77*, 1157–1168. [CrossRef]
78. Rupnik, E.; Daakir, M.; Pierrot Deseilligny, M. MicMac—A Free, Open-Source Solution for Photogrammetry. *Open Geospatial Data, Softw. Stand.* **2017**, *2*, 14. [CrossRef]
79. Sedaghat, A.; Mohammadi, N. High-Resolution Image Registration Based on Improved SURF Detector and Localized GTM. *Int. J. Remote Sens.* **2019**, *40*, 2576–2601. [CrossRef]
80. Stumpf, A.; Malet, J.-P.; Delacourt, C. Correlation of Satellite Image Time-Series for the Detection and Monitoring of Slow-Moving Landslides. *Remote Sens. Environ.* **2017**, *189*, 40–55. [CrossRef]
81. Marsetič, A. Robust Automatic Generation of True Orthoimages from Very High-Resolution Panchromatic Satellite Imagery Based on Image Incidence Angle for Occlusion Detection. *IEEE J. Sel. Top. Appl. Earth Obs. Remote Sens.* **2021**, *14*, 3733–3749. [CrossRef]
82. Yoo, E.J.; Lee, D.-C. True Orthoimage Generation by Mutual Recovery of Occlusion Areas. *GISci. Remote Sens.* **2016**, *53*, 227–246. [CrossRef]
83. Modis, K.; Papaodysseus, K. Theoretical Estimation of the Critical Sampling Size for Homogeneous Ore Bodies with Small Nugget Effect. *Math. Geol.* **2006**, *38*, 489–501. [CrossRef]
84. Carmel, Y.; Dean, D.; Flather, C. Combining Location and Classification Error Sources for Estimating Mult-Temporal Database Accuracy. *Photogramm. Eng. Remote Sens.* **2001**, *67*, 865–872.
85. Guan, L.; Pan, H.; Zou, S.; Hu, J.; Zhu, X.; Zhou, P. The Impact of Horizontal Errors on the Accuracy of Freely Available Digital Elevation Models (DEMs). *Int. J. Remote Sens.* **2020**, *41*, 7383–7399. [CrossRef]
86. Li, W.; Goodchild, M.F. An Optimization Technique for Addressing DEM Misregistration in Hilly Terrain. *Ann. GIS* **2016**, *22*, 43–55. [CrossRef]
87. Livne, E.; Svoray, T. Components of Uncertainty in Primary Production Model: The Study of DEM, Classification and Location Error. *Int. J. Geogr. Inf. Sci.* **2011**, *25*, 473–488. [CrossRef]
88. Mas, J.F. Change Estimates by Map Comparison: A Method to Reduce Erroneous Changes Due to Positional Error. *Trans. GIS* **2005**, *9*, 619–629. [CrossRef]
89. Mi, J.; Liu, L.; Zhang, X.; Chen, X.; Gao, Y.; Xie, S. Impact of Geometric Misregistration in GlobeLand30 on Land-Cover Change Analysis, a Case Study in China. *J. Appl. Remote Sens.* **2022**, 16. [CrossRef]
90. Uhl, J.H.; Leyk, S.; McShane, C.M.; Braswell, A.E.; Connor, D.S.; Balk, D. Fine-Grained, Spatiotemporal Datasets Measuring 200 Years of Land Development in the United States. *Earth Syst. Sci. Data* **2021**, *13*, 119–153. [CrossRef] [PubMed]